Nanoscale

PAPER

View Article Online
View Journal | View Issue

Cite this: *Nanoscale*, 2025, **17**, 8672

Molecular coordination inheritance of single Co atom catalysts for two-electron oxygen reduction reaction†

Qianqian Qin, [a,b] Mengxue Huang,[a,b] Chaoqi Han,[a,b] Xue Jing,[a,b] Wenwen Shi,*[a] Ruiming Ding*[a] and Xi Yin *[a]

Electrosynthesis of hydrogen peroxide (H_2O_2) through the two-electron oxygen reduction reaction (2e-ORR) is environmentally friendly and sustainable. Transition-metal single-atom catalysts (SACs) have gained attention for this application due to their low cost, high atom utilization, adjustable coordination, and geometric isolation of active metal sites. Although various synthetic methods of SACs have been reported, the specific mechanism of the formation of active sites is still less studied. Herein, we presented the molecular coordination inheritance strategy for synthesizing 2e-ORR SACs with well-defined coordination environments and investigated the formation mechanism of the active sites. We select precursors including [Co(II)Salen], CoPc, $Co(acac)_2$ to achieve specific configurations ($Co-N_2O_2$, $Co-N_4$, $Co-O_4$). Our results indicate that the precursors undergo decomposition and are partially embedded in the carbon substrate at lower temperatures, facilitating the inheritance of the desired configurations. As the temperature increases, the inherited configurations will rearrange, forming dual-atom structures and metal particles gradually. Among the $Co-N_2O_2$, $Co-N_4$, and $Co-O_4$ catalysts, the $Co-N_2O_2$ catalyst demonstrates the highest 2e-ORR selectivity. This work reveals the mechanism of regulating SAC's active site structure by the molecular coordination inheritance strategy, which may provide new insights for further research on the precise regulation and formation mechanism of SAC's active site.

Received 23rd January 2025,
Accepted 3rd March 2025

DOI: 10.1039/d5nr00337g

rsc.li/nanoscale

Introduction

Hydrogen peroxide (H_2O_2) is an essential chemical with wide applications in textile bleaching, wastewater treatment, chemical synthesis, and semiconductor cleaning. Currently, its industrial production relies on the anthraquinone method, which requires large-scale equipment and generates large amounts of organic waste.[1,2] The electrochemical production of H_2O_2 *via* a two-electron oxygen reduction reaction (2e-ORR) has emerged as a promising alternative. This method enables on-site production of H_2O_2, thereby simplifying the process and reducing costs while minimizing environmental impact.[3,4] Effective 2e-ORR catalysts are critical for the electrochemical production of H_2O_2. In recent years, carbon-based transition-metal single-atom catalysts (SACs) garnered considerable attention for this application.[5–8] The advantage of transition-metal SACs lies in their low cost, high atom utilization, adjustable coordination, and geometric isolation of active metal sites. The lack of contiguous metal ensemble sites in SACs could prevent the decomposition or further electrochemical reduction of generated H_2O_2.[9–12]

During ORR on SACs, the selectivity towards H_2O_2 or H_2O depends on the tendency of the intermediate *OOH dissociate step.[12–15] To tailor the performance of SACs, changing the metal center atom is a direct method to modulate the adsorption energy of the intermediate on the active site. It has been demonstrated that the cobalt-based SACs own the most promising potential for 2e-ORR.[16–19] Meanwhile, the coordination environment of the metal center atom will affect the electron cloud center and thus change the adsorption of the intermediate. Therefore, tuning the coordination microenvironment can also effectively regulate the performance of the catalyst, such as changing the adjacent coordinative dopants[20–23] and coordination numbers.[24–26]

Currently, various synthesis methods exist to obtain the designed transition-metal SAC for 2e-ORR. Among them, the more common method is to mix metal salts and nitrogen sources with carbon substrates, followed by pyrolysis.[5,26–29] For

[a]*State Key Laboratory of Coal Conversion, Institute of Coal Chemistry, Chinese Academy of Sciences, Taiyuan, Shanxi 030001, China.*
E-mail: shiwenwen@sxicc.ac.cn, dingrm@sxicc.ac.cn, xiyin@sxicc.ac.cn
[b]*School of Chemical Engineering, University of Chinese Academy of Sciences, Beijing 100049, China*

† Electronic supplementary information (ESI) available. See DOI: https://doi.org/10.1039/d5nr00337g

instance, a catalyst with the Co–N_5 sites can be obtained by pyrolysis of mixed cobalt acetate tetrahydrate, triquinoxalinylene, and carbon black.[26] Similarly, the pyrrole-type Co–N_4 catalyst can be obtained by mixing 4-dimethylaminopyridine, cobaltous nitrate hexahydrate, and carbon black after high-temperature heat treatment.[5] Additionally, the method of using carbon substrate and metal complexes with target structures as pyrolysis precursors has also been reported.[21,24] It has also been proved that it is feasible to change the coordination structure of the catalyst by adjusting the pyrolysis atmosphere.[6] However, despite the existence of many methods, achieving precise regulation of the coordination environment of the active site remains a challenge.

Herein, we present the molecular coordination inheritance strategy for synthesizing SACs with well-defined structures and investigate the formation mechanism of the active sites. We studied various precursors, including *N*,*N*′-bis(salicylidene) ethylenediaminocobalt(II) ([Co(II)Salen]), cobalt phthalocyanine (CoPc), and cobalt(II) acetylacetonate ($Co(acac)_2$), to obtain specific configurations: Co–N_2O_2, Co–N_4, and Co–O_4 with Co as the active metal center in each case. Taking the Co–N_2O_2 catalyst as the representative catalyst, we studied the formation mechanism of the catalyst's active site during pyrolysis. We also test the electrochemical performance of Co–N_2O_2, Co–N_4, and Co–O_4 catalysts for 2e-ORR. The result shows the Co–N_2O_2 configuration demonstrates the highest 2e-ORR selectivity, followed by Co–O_4 and then Co–N_4. This work reveals the mechanism of regulating SAC's active site structure by the molecular coordination inheritance strategy, which may provide new insights for further research on the precise regulation and formation mechanism of SAC's active site.

Experimental

Materials

N,*N*′-Bis(salicylidene)ethylenediaminocobalt(II) ([Co(II)Salen], ≥95.0%, Sigma-Aldrich), cobalt phthalocyanine (CoPc, ≥95.0%, Sigma-Aldrich), cobalt(II) acetylacetonate ($Co(acac)_2$, ≥99.0%, Sigma-Aldrich), nitric acid (HNO_3, 65–68 wt%, analytical reagent grade, SCR), methanol (MeOH, >99.7%, analytical reagent grade, Kermel), isopropanol (IPA, >99.7%, analytical reagent grade, Kermel), hydrogen peroxide solution (H_2O_2, 30 wt%, analytical reagent grade, Alfa Aesar), perchloric acid ($HClO_4$, analytical reagent grade, Alfa Aesar), deionized water (DI water, Milli-Q, 18.2 MΩ cm at 25 °C), ultrapure nitrogen (N_2, 99.999%), ultrapure oxygen (O_2, 99.999%), carbon black (BlackPearl 2000, Cabot Co.), and a Nafion D521 dispersion (5 wt%, EW = 1100, Alfa Aesar) were used as received.

Synthesis of the [Co(II)Salen]-OCB-*T* °C catalyst

Oxidized carbon black (OCB) was first prepared by oxidizing 10.0 g of carbon black in 500 mL of 70% HNO_3 for 8 h at 80 °C, rinsed with DI water, vacuum dried at 80 °C, and used as the carbon source in the synthesis. 240 mg of OCB was dispersed in 180 mL of methanol and subjected to ultrasonication at 25 °C for 1 h. [Co(II)Salen] (63 mg, 193.7 mmol) was dissolved into 60 mL methanol and stirred constantly at 60 °C for 1 h. Subsequently, OCB dispersion was mixed with the [Co(II)Salen] solution and underwent ultrasonication for 1 h, followed by stirring at 500 rpm at 25 °C for 24 h. The dispersion was filtered, and the resulting solid was dried under vacuum at 60 °C. The dried powder was loaded into an alumina combustion boat and heat-treated at *T* °C in a tube furnace in N_2 at 1 L min^{-1} (*T* = 300, 500, 700, and 900, respectively). The ramping rate was 30 °C min^{-1}, and the holding time at *T* °C was one hour. The obtained product was the [Co(II)Salen]-OCB-*T* °C catalyst. When *T* = 300, the obtained catalyst ([Co(II)Salen]-OCB-300 °C) was the Co–N_2O_2 catalyst.

Synthesis of the [Co(II)Salen]-OCB catalyst

The [Co(II)Salen]-OCB catalyst was prepared by using the same synthesis method as the Co–N_2O_2 catalysts but without the pyrolysis step.

Synthesis of the Co–N_4 catalyst

The Co–N_4 catalyst was prepared by using the same synthesis method as the Co–N_2O_2 catalyst, except that the precursor molecule was CoPc (94.8 mg, 165.9 mmol) with the pyrolysis temperatures of 700 °C.

Synthesis of the Co–O_4 catalyst

The Co–O_4 catalyst was prepared by using the same synthesis method as the Co–N_2O_2 catalyst, except that the precursor molecule was $Co(acac)_2$ (42.7 mg, 166.1 mmol) with the pyrolysis temperatures of 300 °C.

Characterization

Powder X-ray diffraction (XRD) was performed on a Bruker D8 ADVANCE A25 using Cu Ka radiation over a 2θ range from 10° to 80°. The morphological information was examined with transmission electron microscopy (TEM, JEOL JEM-2100F). X-ray absorption fine structure measurements were carried out on the soft X-ray spectroscopy beamline at the Beijing Synchrotron Radiation Facility and Shanghai Synchrotron Radiation Facility. The end station was equipped with a hemispherical electron analyzer and a microchannel plate detector that enabled simultaneous recording of total electron yield and partial electron yield data. X-ray photoelectron spectroscopy (XPS, Axis Ultra DLD X-ray photoelectron spectrometer, Kratos Analytical Ltd, UK) was performed using a monochromatic Al Kα source at 150 W without charge compensation. Raman spectra were recorded on a Horiba LabRAM HR Evolution Raman spectrometer using 514 nm laser as the excitation source. Fourier transform infrared (FTIR) was performed on a Thermo Fisher Scientific Nicolet iS20.

Electrochemical measurements

Electrochemical measurements were conducted using a three-electrode system controlled by a Pine Research MSR rotator (Pine Research Instrumentation Co. Ltd) and a bipotentiostat (CHI 760E, CH Instruments, Inc.). A five-necked electro-

chemical cell filled with 0.1 M $HClO_4$ solution was used in the experiment. A rotating-ring disk electrode (RRDE, Pine Research Instrumentation) with a glassy carbon electrode (GCE, area = 0.2475 cm^2) and a Pt-ring electrode (area = 0.1866 cm^2) was used as the working electrode. An Ag/AgCl (sat. KCl) electrode and graphite rod were used as the reference and counter electrode, respectively. The Ag/AgCl electrode was calibrated to a reversible hydrogen electrode (RHE), which was constructed by bubbling pure H_2 gas continuously onto a Pt coil electrode placed in a glass tube filled with 0.1 M $HClO_4$.

The catalyst ink was prepared by dispersing 5 mg of catalyst in a mixture of DI-water (500 μL), IPA (500 μL), and D521 Nafion dispersion (10 μL, 5 wt%) in a sonication bath for one hour. Then, electrodes with a catalyst loading of 0.12 mg cm^{-2} were prepared by depositing 10 μL of the ink onto the GCE on the RRDE.

Cyclic voltammograms (CV) were recorded from 0.0 to 1.0 V *vs.* RHE at a scan rate of 50 mV s^{-1} in N_2-saturated 0.1 M $HClO_4$ solution. Linear sweep voltammetry (LSV) measurements were conducted in O_2-saturated conditions between 0.0 and 1.0 V at a scan rate of 5.0 mV s^{-1} at 1600 rpm. To detect the produced H_2O_2, a fixed potential of 1.3 V *vs.* RHE was applied to the Pt-ring electrode. All the polarization curves were corrected with 90% iR-compensation.

The collection efficiency (N) of the Pt-ring electrode was measured to be 37%. The H_2O_2 selectivity (H_2O_2%) and the stoichiometric number of transferred electrons (n) in the ORR were calculated from the disk current (I_d) and ring current (I_r) results based on the following equations:

$$H_2O_2(\%) = 200\frac{\left(\frac{I_r}{N}\right)}{\left(I_d + \frac{I_r}{N}\right)} \quad (1)$$

$$n = \frac{\left(\frac{I_r}{N}\right)}{\left(I_d + \frac{I_r}{N}\right)} \quad (2)$$

The kinetically limited current density (j_k) was determined using the Koutecký–Levich equation:

$$\frac{1}{j} = \frac{1}{j_k} + \frac{1}{j_L} \quad (3)$$

where j is the measured current density and j_L is the diffusion-limited current density. The j_L is obtained by the equation:

$$j_L = 0.62nFC_{O_2}D_{O_2}^{\frac{2}{3}}\nu^{-\frac{1}{6}}\omega^{\frac{1}{2}} \quad (4)$$

where n is the stoichiometric number of electrons transferred in the ORR, F is the Faraday constant (96 485 C mol^{-1}), A is the electrode area, C_{O_2} is the concentration of dissolved O_2 (1.26 × 10^{-3} mol L^{-1} in 0.1 M $HClO_4$), D_{O_2} is the diffusion coefficient (1.93 × 10^{-5} cm^2 s^{-1} in 0.1 M $HClO_4$), ν is the kinetic viscosity of the solution (1.009 × 10^{-2} cm^2 s^{-1} in 0.1 M $HClO_4$), and ω is the rotation rate of the disc electrode.

Results and discussion

Molecular coordination inheritance strategy for the synthesis of the well-defined Co–N_2O_2, Co–N_4, and Co–O_4 sites

We present the molecular coordination inheritance strategy, especially for the precise synthesis of well-defined Co–N_2O_2, Co–N_4, and Co–O_4 sites with detailed characterization analysis. Fig. 1 illustrates this molecular coordination inheritance strategy. [Co(II)Salen], CoPc, and $Co(acac)_2$ were selected as the precursor molecules due to their well-defined coordination structure, which provides the necessary ligands that form a precise coordination environment with the Co atom center. After the precursor molecules are uniformly distributed across the substrate, pyrolysis is taken to break down part of the organic structure while inheriting or preserving the Co–N_2O_2, Co–N_4, and Co–O_4 configurations. Combined with the thermogravimetric analysis results of the three precursor molecules (Fig. S1†), the pyrolysis temperatures of 300 °C, 300 °C, and 700 °C were selected to achieve this effect.

Fig. 2 presents the results of the structural and elemental analysis for the Co–N_2O_2, Co–N_4, and Co–O_4 catalysts. The TEM image (Fig. 2a) reveals only carbon nanoparticles without noticeable metal particles. The XRD patterns (Fig. 2b) show only broad peaks associated with the (002) and (100) reflections of graphitized carbon.

Notably, there are no diffraction peaks indicative of metal, metal nitride, or metal oxide. This observation suggests that any cobalt present in three samples is highly dispersed or in an amorphous state, consistent with the TEM results.[5,30] The XPS analysis (Table S1†) suggests that three catalysts own similar Co doping content of approximately 0.5 atom%. The content of O in Co–N_2O_2, Co–N_4, and Co–O_4 catalysts is 7.58%, 2.75%, and 8.36%, and the content of N in Co–N_2O_2 and Co–N_4 catalysts is 1.97% and 3.87%, respectively. No significant signal of the N element is present in the Co–O_4 catalyst (Fig. S2†).

The N 1s XPS spectra (Fig. 2c and Table S2†) for Co–N_2O_2 and Co–N_4 catalysts can be fitted with five main types of N species: pyridinic-N, Co–N_x, pyrrolic-N, graphitic N, and oxidized N.[29,31,32] Compared to the Co–N_4 catalyst, the binding energy peak centers of pyridinic-N and Co–N_x in the Co–N_2O_2

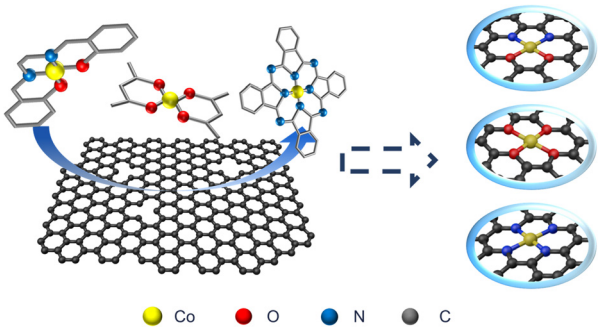

Fig. 1 Schematic illustration of the molecular coordination inheritance strategy design.

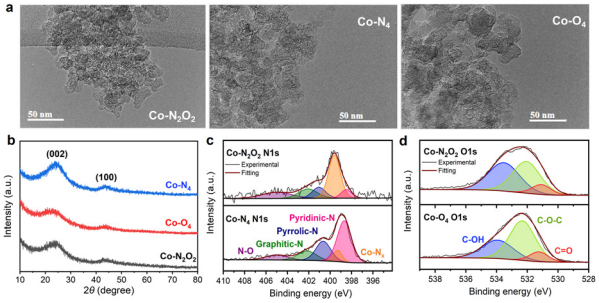

Fig. 2 (a) TEM micrographs and (b) XRD patterns of Co–N_2O_2, Co–N_4, Co–O_4 catalysts. (c) N 1s XPS spectra of Co–N_2O_2 and Co–N_4 catalyst. (d) O 1s XPS spectra of Co–N_2O_2 and Co–O_4 catalyst.

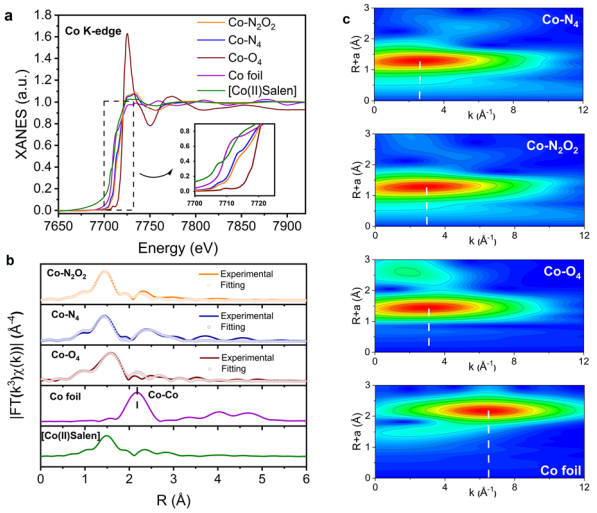

Fig. 3 (a) Co K-edge XANES spectra and (b) FT k^2-weighted and fitting EXAFS spectra of the Co–N_2O_2, Co–N_4, Co–O_4 catalysts, and Co foil, [Co(II)Salen] as reference. (c) Wavelet transform (WT) k^2-weighted EXAFS contour plots of the Co–N_4, Co–N_2O_2, Co–O_4 catalysts, and Co foil as reference.

catalyst exhibit a noticeable shift to higher binding energies obviously (>0.2 eV). This difference is attributed to the distinct chemical environments of the N species in the two catalysts. In the Co–N_2O_2 configuration, the O atom possesses a stronger electron-accepting ability, leading to fewer electrons being received by the N atoms. The O atoms reduce the electron density on the neighboring N atoms in the Co–N_2O_2, whereas in the Co–N_4 catalyst, the N atoms fully retain electrons donated by the Co atom. In addition, the proportions of N species (Fig. S3†) in the Co–N_2O_2 and Co–N_4 catalysts are very different. The relative content of pyrrolic-N in the Co–N_2O_2 catalyst is greater than that of pyridinic-N, while the relative content of pyridinic-N in the Co–N_4 catalyst is higher.

The O 1s XPS spectra (Fig. 2d) of Co–N_2O_2 and Co–O_4 catalyst can be deconvoluted into three peaks: hydroxyl groups (C–OH), etheric groups (C–O–C), and carbonyl groups (C═O).[27,33] Compared with Co–N_2O_2 catalyst, the binding energy peak centers of C–OH and C–O–C of Co–O_4 catalyst are shifted to higher binding energy obviously (>0.2 eV) (Table S3†). Similarly, the reason is that the O atom in the Co–N_2O_2 catalyst gained more electrons than the N atom due to the larger electronegativity of O, which increases the electron density on the O atom in the Co–N_2O_2 catalyst. The relative content of C–O–C in Co–O_4 is higher than that of Co–N_2O_2 catalyst (Fig. S4†), since the C–O–C bond results from the bonding between the O atom at the active site and the carbon substrate. The above structural and elemental analysis results indicate that three catalysts are primarily carbon matrices doped with atomically dispersed Co and N/O elements. The electron distribution state and coordination environment of the Co center between the three catalysts are completely different.

X-ray absorption spectroscopy (XAS) was further used to determine the chemical states and local coordination environment of the Co atom in three SACs. In the Co K-edge X-ray absorption near-edge structure (XANES) spectra (Fig. 3a), the pre-edge absorption energy of the Co–N_2O_2 catalyst is higher than the Co foil, indicating the positive valency of Co. The absorption edge of the Co–N_2O_2 catalyst is lower than the Co–O_4 catalyst but higher than the Co–N_4 catalyst since N is less electronegative than O. The Fourier-transformed extended X-ray absorption fine structure (FT-EXAFS) spectra (Fig. 3b) indicate the absence of Co–Co bonds (~2.17 Å) in the three catalysts, further confirming the single-atom dispersion of Co. The prominent peaks of Co–O_4 (1.60 Å), Co–N_4 (1.44 Å), and Co–N_2O_2 (1.44 Å) catalysts are attributed to Co–O, Co–N, Co–N/Co–O bonds, respectively. The prominent peaks in Co–N_2O_2 and Co–N_4 catalysts are close because the length of the Co–N and Co–O bonds in the precursor molecule [Co(II)Salen] are similar to the Co–N bonds in the CoPc molecule (Fig. S5 and Table S4†).

The local coordination configuration was further studied by quantitative least squares EXAFS curve fitting analysis, and the detailed fitting parameters are shown in Table S5.† According to the fitted parameters, the best-fitting result of Co–N_2O_2 for the first coordination sphere of Co includes two backscattering paths: Co–O and Co–N. The coordination numbers for Co–N and Co–O are both approximately 2, and the fitted bond lengths of Co–N and Co–O are 1.86 and 1.87 Å, respectively. For Co–N_4 and Co–O_4 catalysts, the coordination numbers of N and O are both approximately 4, and the fitted bond lengths of Co–N and Co–O are 1.89 and 1.88 Å, respectively. The wavelet-transform (WT) EXAFS analysis (Fig. 3c) further elucidates the differences in the coordination environments across the samples. In WT-EXAFS analysis, lighter atoms show the strongest oscillations at low k positions, while heavier atoms peak at high k. The Co–N_4, Co–N_2O_2, and Co–O_4 catalysts exhibit intensity maximum of 2.6, 2.9, and 3.1 $Å^{-1}$ respectively, which can be assigned to the backscattering of Co–N, Co–N/Co–O, and Co–O bonds. Since the atomic number of O is greater than N, the intensity maximum of the Co–N_2O_2 catalyst is between the Co–N_4 and Co–O_4 catalyst, consistent with the fitted coordination numbers. Meanwhile, the XPS analysis result showed that the contents of N and O elements in the two catalysts

were very different, which also confirmed our conclusion. Summarizing the above results, we have experimentally obtained the catalysts featuring well-defined Co–N_2O_2, Co–N_4, and Co–O_4 sites, confirming the effectiveness of the molecular coordination inheritance strategy.

Pyrolysis mechanism in molecular coordination inheritance strategy

We investigate the pyrolysis process within the molecular coordination inheritance strategy represented by [Co(II)Salen]-OCB precursor. Fig. 4a presents the cyclic voltammograms (CV) of the OCB substrate, [Co(II)Salen]-OCB precursor, and Co–N_2O_2 ([Co(II)Salen]-OCB-300 °C) catalyst. After heat treatment at 300 °C, the peak in *area 3* is retained, which corresponds to the redox reaction of the quinone functional groups in OCB substrates. In contrast, the redox peaks in *areas 1* and *2*, attributed to the [Co(II)Salen]-OCB precursor, only preserve peaks in *area 2*. We speculated that the missing redox peaks in *area 1* came from a part of the hydrocarbon organic functional group of the precursor [Co(II)Salen], and the decomposition of which after pyrolysis led to the disappearance of the peak. The retained redox peaks in *area 2* are likely derived from the –N_2O_2 coordination structure around the Co atom, suggesting that the Co–N_2O_2 structure was probably directly inherited from the precursor.

Fig. 4b presents FTIR spectra of OCB, [Co(II)Salen]-OCB, and Co–N_2O_2 catalysts. The peak (yellow region) ranging from 1760 cm^{-1} to 1650 cm^{-1} corresponds to carboxylic acid (–COOH), while the peaks (pink region) around 1500 cm^{-1} are attributed to the skeleton vibration of sp^2-hybridized C=C bond. The peak (purple region) at 1100 to 1030 cm^{-1} represents the asymmetric stretching vibration of the C–O–C group, and the peaks (blue region) at 770 cm^{-1} to 730 cm^{-1} arise from the out-of-plane bending or twisting of the hydrocarbons group (–CH).[34–37] A careful analysis of the peaks across the three spectra reveals that after heat treatment, the broad peak (purple region, 1100 cm^{-1}–1030 cm^{-1}) corresponding to the asymmetric stretching vibration of the C–O–C group appears exclusively in the Co–N_2O_2 catalyst. This result indicates that the Co–N_2O_2 site is chemically bonded to the carbon framework after pyrolysis, as depicted in Fig. 4c, rather than the precursor molecule simply adsorbed onto the carbon substrate. Furthermore, the –COOH, –C=C, and –CH groups in the precursor remain after heat treatment, indicating that the catalyst retains part of the precursor structure.

The Raman spectrum of the OCB substrate, [Co(II)Salen]-OCB precursor, and Co–N_2O_2 catalyst (Fig. S6†) includes two peaks of D-band (1350 cm^{-1}) and G-band (1580 cm^{-1}), which were assigned to the sp^3 and sp^2-hybridized carbon. The ratio of the relative intensity of D and G bands (I_D/I_G) in carbon-based nanocomposites indicates the disorder content in the graphitic structure and structural defects, which are likely to influence the performance of the catalysts.[8] The I_D/I_G ratio of the OCB substrate, [Co(II)Salen]-OCB precursor, and Co–N_2O_2

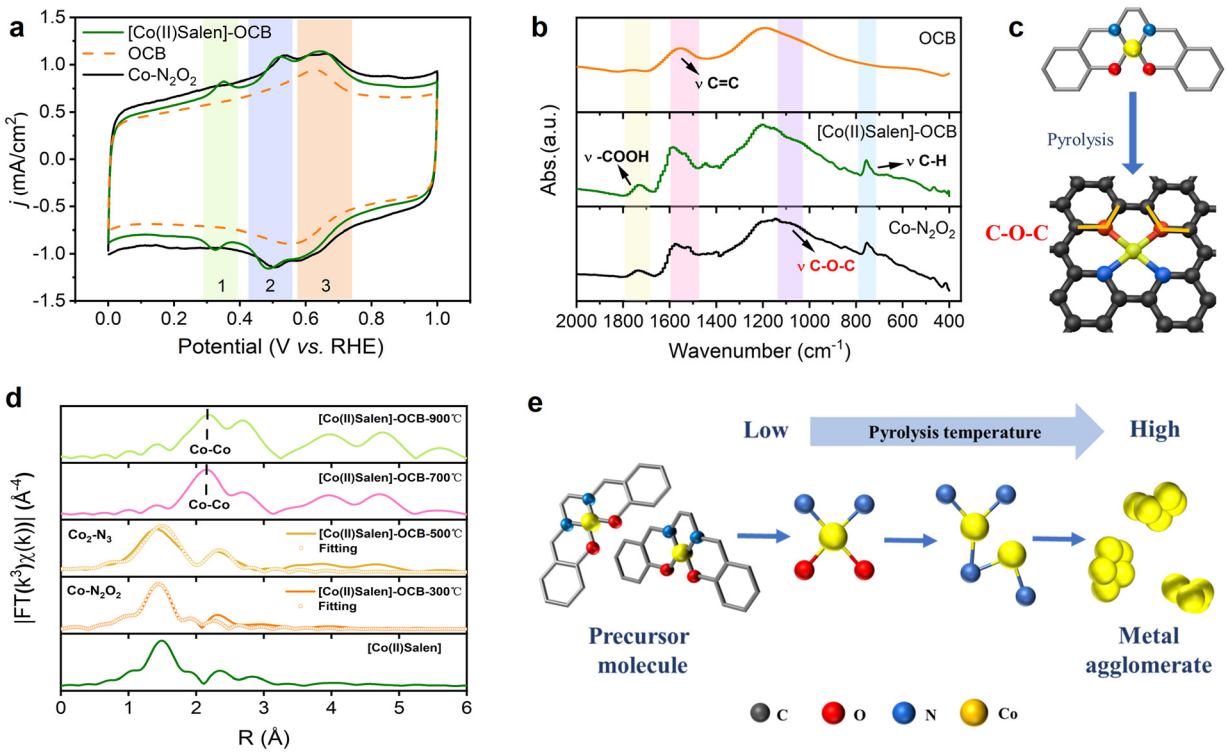

Fig. 4 (a) The cyclic voltammetry curves and (b) FTIR spectra of OCB, [Co(II)Salen]-OCB, and Co–N_2O_2 catalysts. (c) Schematic illustration of the mechanism of the Co–N_2O_2 site bonding to the carbon substrate after pyrolysis. (d) FT k_2-weighted and fitting EXAFS spectra of the [Co(II)Salen]-OCB-*T* °C catalysts (*T* = 300, 500, 700, 900). (e) Schematic illustration of the pyrolysis process of [Co(II)Salen] molecules on carbon substrate.

catalyst were similar, suggesting that precursor loading and pyrolysis won't significantly change the carbon substrate's graphitic structure and structural defects. The polarization curve of the OCB substrate, [Co(II)Salen]-OCB precursor, and Co–N_2O_2 catalyst showed apparent differences (Fig. S7†), suggesting that the chemical bond formed by low pyrolysis temperature plays a vital role in the activity.

We further investigate the evolution of the [Co(II)Salen]-OCB precursor at elevated temperatures, as shown in Fig. 4d. The parameters related to the best EXAFS fitting results are shown in Table S5.† Through quantitative least squares EXAFS curve fitting analysis, the optimal fitting result for the sample pyrolyzed at 500 °C reveals two backscattering paths: Co–N and Co–Co. The coordination number of Co in the first coordination sphere of Co is approximately 1. For the samples pyrolyzed at 700 °C and 900 °C, the pronounced peaks at 2.17 Å belong to the Co–Co bond, indicating the presence of Co metal agglomerates. This fitting result suggests that with pyrolysis at 500 °C, the Co–O bond is almost completely broken, and the Co–N bond is partially retained. The distribution of metal atoms begins to reorganize and gradually move closer to each other, and the coexistence of single-atom structure and dual-atom structure appears. When the pyrolysis temperature increases to 700 °C and above, the Co–N bond is further broken, and more metal atoms gather to form agglomeration.

Based on the results presented above, the pyrolysis process of [Co(II)Salen] molecules on the carbon substrate, as we speculate, is illustrated in Fig. 4e. At lower heat treatment temperatures, the Co–N_2O_2 structure of the [Co(II)Salen] molecule is partially inherited and embedded within the carbon substrate. As the pyrolysis temperature increases, the Co–N and Co–O bonds gradually break, and the distribution of metal atoms begins to reorganize. The metal atoms gradually change from the initial single atomic state to the diatomic structure and finally to the metal agglomeration. After pyrolysis at higher temperatures, more metal atoms aggregate to form Co metal clusters or particles. This result demonstrates that the Co–N_2O_2 structure in [Co(II)Salen] molecules is preserved at low pyrolysis temperature, and the active site of the Co–N_2O_2 catalyst is directly inherited from the precursor.

Electrochemical performance

Following the synthesis of well-defined Co–N_2O_2, Co–N_4, and Co–O_4 sites, we analyzed the relationship between their configurations and the corresponding 2e-ORR activity. As illustrated in Fig. 5a, the significant shift in polarization curves upon the introduction of SCN^- ions indicate a substantial decrease in the ORR activity of all three catalysts. This result suggested that the Co atom acts as the actual active center in these catalysts since SCN^- ions can strongly bind to the single metal atom, which would block that metal site for O_2 adsorption.[38,39]

Fig. 5b and c show the polarization curves, the corresponding H_2O_2 selectivity, and electron transfer number (n) as a function of applied potential. The Co–N_2O_2 catalyst exhibits an onset potential of 0.684 V *vs.* RHE (defined as the potential

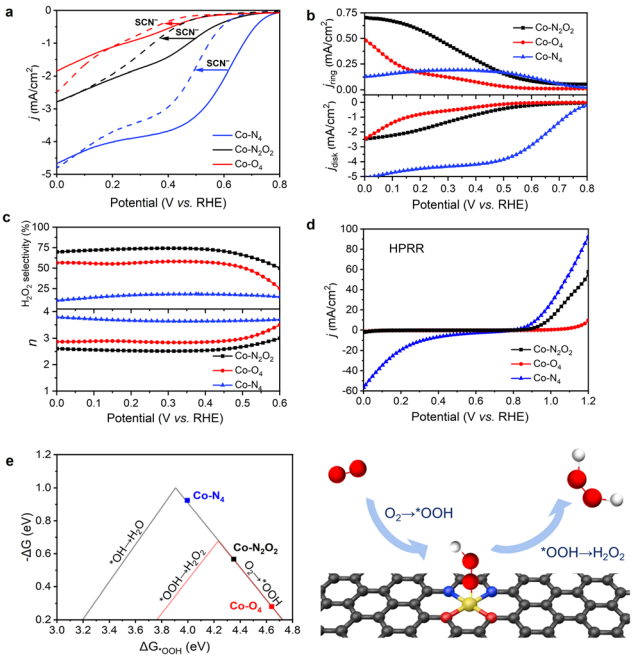

Fig. 5 (a) Polarization curves of the Co–N_2O_2, Co–N_4, and Co–O_4 catalysts in O_2-saturated 0.1 M $HClO_4$ (with and without 5 mM SCN^- ions). (b) Linear sweep voltammetry curves recorded at 1600 rpm and a scan rate of 5 mV s^{-1} in O_2-saturated 0.1 M $HClO_4$, together with the detected H_2O_2 currents density on the ring electrode at a fixed potential of 1.3 V *vs.* RHE. (c) The calculated H_2O_2 selectivity and electron transfer number n during LSV scan. (d) Polarization curves of the Co–N_2O_2, Co–N_4, and Co–O_4 catalysts in N_2-saturated 0.5 M H_2SO_4 electrolyte containing 0.5 M H_2O_2. (e) Calculated catalytic volcanoes for the production of H_2O (black lines) and H_2O_2 (red lines) *via* ORR with the schematic illustration of the structure active site. The values of the *OOH adsorption energy (ΔG_{*OOH}) and the free energy change along each ORR step ($-\Delta G$) are obtained from the literature.[40]

delivering 0.1 mA cm^{-2} current density) and a j_L of −2.5 mA cm^{-2}. The calculated selectivity of H_2O_2 is up to 76% with an n value of 2.5, indicating that the ORR on the Co–N_2O_2 surface is predominantly a 2e-process. In contrast, the Co–N_4 catalyst displays an onset potential of 0.91 V *vs.* RHE and a j_L of about −5 mA cm^{-2}. The H_2O_2 selectivity for Co–N_4 is 16%, and its n is close to 3.7, suggesting a 4e-ORR pathway. This result is consistent with existing studies that the Co SAC catalyst with the pyridine-type CoN_4 active site is more inclined to facilitate 4e-path ORR, as XPS shows that the main N species in Co–N_4 catalyst is pyridinic-N.[5] The onset potential of the Co–O_4 catalyst is 0.521 V *vs.* RHE, and the j_L is not reached. The calculated H_2O_2 selectivity and n for the Co–O_4 catalyst are about 58% and 2.9 respectively, showing a mixed 2e- and 4e-ORR pathway. The results show that the Co–N_2O_2 catalyst showed much better 2e-ORR performance than the Co–N_4, Co–O_4 catalysts. The electrochemical performance of the [Co(II)Salen]-OCB-T °C catalysts (T = 500, 700, 900) was also tested (Fig. S8†), revealing lower 2e-ORR selectivity compared to the Co–N_2O_2 catalyst. This performance degradation arises from the fact that high-temperature-induced coordination recon-

struction at metal centers generates heterogeneous active sites, thereby driving a transition from dominant 2e-ORR to mixed 2e-/4e-ORR pathways.

The catalytic activity of these catalysts toward the H_2O_2 reduction reaction (HPRR) was also evaluated.[41,42] As shown in Fig. 5d, the negligible current density of Co–N_2O_2 and Co–O_4 catalysts indicate the poor HPRR activity of these two catalysts. Meanwhile, the Co–N_4 catalyst exhibits much better HPRR activity with significant current density. This result suggests that H_2O_2 generated by Co–N_2O_2 and Co–O_4 catalysts will hardly be reduced, while the Co–N_4 catalyst is likely to further reduce H_2O_2 to H_2O. The difference in HPRR activity also explains why Co–N_2O_2 is more inclined to 2e-ORR and Co–N_4 is more inclined to 4e-ORR. The Co–N_2O_2 catalyst was also evaluated in an H-cell configuration (Fig. S9†), demonstrating significant initial current density that highlights its practical potential for applications. Further investigations will systematically explore the optimization of the triple-phase boundary and mass transfer efficiency to enhance its performance under operational conditions.

In short, the electrochemical performance shows that the Co–N_2O_2 configuration demonstrates the highest 2e-ORR selectivity, followed by Co–O_4 and then Co–N_4. According to the recent study, the superior 2e-ORR performance of the Co–N_2O_2 catalyst can be attributed to the synergistic interplay between the electronic state of the Co center and its coordination environment.[40] As shown in Fig. 5e, the density functional theory (DFT) calculations reveal that the Co–N_2O_2 configuration is positioned closer to the top of the volcano plot compared to the Co–N_4 and Co–O_4 structures, which accounts for its enhanced 2e-ORR activity.

Conclusions

In summary, we presented the molecular coordination inheritance strategy for synthesizing SACs with well-defined coordination environments and investigated the formation mechanism of the active sites. We selected precursors including [Co(II) Salen], CoPc, and $Co(acac)_2$ to achieve specific configurations (Co–N_2O_2, Co–N_4, Co–O_4). Taking the Co–N_2O_2 catalyst as the representative catalyst, our investigations into the pyrolysis mechanism reveal that the precursors undergo decomposition and are partially embedded in the carbon substrate at lower temperatures, facilitating the inheritance of the desired configurations. As the temperature increases, the inherited configurations will rearrange, forming dual-atom structures and metal particles. Following the successful synthesis of these well-defined sites, we analyzed the relationship between their configurations and their 2e-ORR activity. Our findings indicate that the Co–N_2O_2 configuration demonstrates the highest 2e-ORR selectivity, followed by Co–O_4 and then Co–N_4. This work reveals the mechanism of regulating SAC's active site structure by the molecular coordination inheritance strategy, which may provide new insights for further research on the precise regulation and formation mechanism of SAC's active site.

Author contributions

Qianqian Qin: writing – original draft, methodology, investigation, visualization. Mengxue Huang: investigation. Chaoqi Han: investigation. Xue Jing: investigation. Wenwen Shi: writing – original draft, methodology. Ruimin Ding: writing – review & editing, supervision, funding acquisition. Xi Yin: writing – review & editing, conceptualization, methodology, supervision, funding acquisition.

Data availability

The data supporting this article have been included as part of the ESI.†

Conflicts of interest

There are no conflicts to declare.

Acknowledgements

This study was financially supported by the National Key Research and Development Program of China (2021YFB4001203), the Fundamental Research Program of China Postdoctoral Science Foundation (Grant No. 2022M723263), the State Key Laboratory of Coal Conversion, Institute of Coal Chemistry, Chinese Academy of Sciences (Grant No. SCJC-HN-2023-16, SCJC-HN-2023-17). The authors wish to thank the facility's support of the BL14W1 station in the Shanghai Synchrotron Radiation Facility (SSRF) and the 1 W1B station in the Beijing Synchrotron Radiation Facility (BSRF) for the collection of XAFS data.

References

1 J. M. Campos-Martin, G. Blanco-Brieva and J. L. G. Fierro, *Angew. Chem., Int. Ed.*, 2006, **45**, 6962–6984.
2 S. C. Perry, D. Pangotra, L. Vieira, L. I. Csepei, V. Sieber, L. Wang, C. P. de León and F. C. Walsh, *Nat. Rev. Chem.*, 2019, **3**, 442–458.
3 S. Yang, A. Verdaguer-Casadevall, L. Arnarson, L. Silvio, V. Colic, R. Frydendal, J. Rossmeisl, I. Chorkendorff and I. E. L. Stephens, *ACS Catal.*, 2018, **8**, 4064–4081.
4 X. Zhang, Y. Xia, C. Xia and H. T. Wang, *Trends Chem.*, 2020, **2**, 942–953.
5 S. Y. Chen, T. Luo, X. Q. Li, K. J. Chen, J. W. Fu, K. Liu, C. Cai, Q. Y. Wang, H. M. Li, Y. Chen, C. Ma, L. Zhu, Y. R. Lu, T. S. Chan, M. S. Zhu, E. Cortes and M. Liu, *J. Am. Chem. Soc.*, 2022, **144**, 14505–14516.
6 C. Tang, L. Chen, H. J. Li, L. Q. Li, Y. Jiao, Y. Zheng, H. L. Xu, K. Davey and S. Z. Qiao, *J. Am. Chem. Soc.*, 2021, **143**, 7819–7827.

7 X. Q. Wang, Z. J. Li, Y. T. Qu, T. W. Yuan, W. Y. Wang, Y. Wu and Y. D. Li, *Chem*, 2019, **5**, 1486–1511.
8 S. Zhang, Z. Tao, M. Y. Xu, L. Kan, C. P. Guo, J. M. Liu, L. H. He, M. Du and Z. H. Zhang, *Small*, 2024, **20**, 11.
9 J. J. Gao and B. Liu, *ACS Mater. Lett.*, 2020, **2**, 1008–1024.
10 J. H. Kim, Y. T. Kim and S. H. Joo, *Curr. Opin. Electrochem.*, 2020, **21**, 109–116.
11 M. M. Liu, L. L. Wang, K. N. Zhao, S. S. Shi, Q. S. Shao, L. Zhang, X. L. Sun, Y. F. Zhao and J. J. Zhang, *Energy Environ. Sci.*, 2019, **12**, 2890–2923.
12 M. Song, W. Liu, J. J. Zhang, C. Zhang, X. Huang and D. L. Wang, *Adv. Funct. Mater.*, 2023, **33**, 17.
13 J. J. Lu, P. J. Deng, G. L. Fu, X. Y. Meng, S. R. Zhang and B. C. Yang, *ChemElectroChem*, 2024, **11**, 17.
14 K. Sun, W. W. Xu, X. Lin, S. B. Tian, W. F. Lin, D. J. Zhou and X. M. Sun, *Adv. Mater. Interfaces*, 2021, **8**, 16.
15 H. Yin, R. L. Pan, M. M. Zou, X. Ge, C. X. Shi, J. L. Yuan, C. J. Huang and H. B. Xie, *Nanomaterials*, 2024, **14**, 14.
16 J. J. Gao, H. B. Yang, X. Huang, S. F. Hung, W. Z. Cai, C. M. Jia, S. Miao, H. M. Chen, X. F. Yang, Y. Q. Huang, T. Zhang and B. Liu, *Chem*, 2020, **6**, 658–674.
17 C. Liu, H. Li, F. Liu, J. S. Chen, Z. X. Yu, Z. W. Yuan, C. J. Wang, H. L. Zheng, G. Henkelman, L. Wei and Y. Chen, *J. Am. Chem. Soc.*, 2020, **142**, 21861–21871.
18 Y. Y. Sun, L. Silvioli, N. R. Sahraie, W. Ju, J. K. Li, A. Zitolo, S. Li, A. Bagger, L. Arnarson, X. L. Wang, T. Moeller, D. Bernsmeier, J. Rossmeisl, F. Jaouen and P. Strasser, *J. Am. Chem. Soc.*, 2019, **141**, 12372–12381.
19 C. Z. Ye, Y. F. Zhou, H. Y. Li and Y. Shen, *Green Chem.*, 2023, **25**, 3931–3939.
20 C. Tang, Y. Jiao, B. Y. Shi, J. N. Liu, Z. H. Xie, X. Chen, Q. Zhang and S. Z. Qiao, *Angew. Chem., Int. Ed.*, 2020, **59**, 9171–9176.
21 Y. H. Tian, M. Li, Z. Z. Wu, Q. Sun, D. Yuan, B. Johannessen, L. Xu, Y. Wang, Y. H. Dou, H. J. Zhao and S. Q. Zhang, *Angew. Chem., Int. Ed.*, 2022, **61**, 9.
22 Y. H. Wu, Y. F. Ding, X. Han, B. B. Li, Y. F. Wang, S. Y. Dong, Q. L. Li, S. X. Dou, J. Y. Sun and J. H. Sun, *Appl. Catal., B*, 2022, **315**, 10.
23 L. J. Yang, G. Sun, H. L. Fu and L. Zhang, *Chem. Eng. J.*, 2023, **472**, 9.
24 Y. L. Wang, R. Shi, L. Shang, G. I. N. Waterhouse, J. Q. Zhao, Q. H. Zhang, L. Gu and T. R. Zhang, *Angew. Chem., Int. Ed.*, 2020, **59**, 13057–13062.
25 H. B. Xu, H. X. Jia, H. Z. Li, J. Liu, X. W. Gao, J. C. Zhang, M. Liu, D. L. Sun, S. L. Chou, F. Fang and R. B. Wu, *Appl. Catal., B*, 2021, **297**, 9.
26 Q. L. Zhao, Y. Wang, W. H. Lai, F. Xiao, Y. X. Lyu, C. Z. Liao and M. H. Shao, *Energy Environ. Sci.*, 2021, **14**, 5444–5456.
27 E. Jung, H. Shin, B. H. Lee, V. Efremov, S. Lee, H. S. Lee, J. Kim, W. Hooch Antink, S. Park, K. S. Lee, S. P. Cho, J. S. Yoo, Y. E. Sung and T. Hyeon, *Nat. Mater.*, 2020, **19**, 436–442.
28 W. Wang, Y. C. Hu, P. Li, Y. C. Liu and S. L. Chen, *ACS Catal.*, 2024, **14**, 5961–5971.
29 H. Xu, S. B. Zhang, J. Geng, G. Z. Wang and H. M. Zhang, *Inorg. Chem. Front.*, 2021, **8**, 2829–2834.
30 Z. Y. Lu, G. X. Chen, S. Siahrostami, Z. H. Chen, K. Liu, J. Xie, L. Liao, T. Wu, D. C. Lin, Y. Y. Liu, T. F. Jaramillo, J. K. Norskov and Y. Cui, *Nat. Catal.*, 2018, **1**, 156–162.
31 G. B. Chen, Y. An, S. W. Liu, F. F. Sun, H. Y. Qi, H. F. Wu, Y. H. He, P. Liu, R. Shi, J. Zhang, A. Kuc, U. Kaiser, T. R. Zhang, T. Heine, G. Wu and X. L. Feng, *Energy Environ. Sci.*, 2022, **15**, 2619–2628.
32 H. L. Huang, M. Z. Sun, S. W. Li, S. B. Zhang, Y. Y. Lee, Z. W. Li, J. J. Fang, C. J. Chen, Y. X. Zhang, Y. F. Wu, Y. Z. Che, S. R. Qian, W. Zhu, C. Tang, Z. B. Zhuang, L. Zhang and Z. Q. Niu, *J. Am. Chem. Soc.*, 2024, **146**, 9434–9443.
33 H. S. Gong, Z. X. Wei, Z. C. Gong, J. J. Liu, G. L. Ye, M. M. Yan, J. C. Dong, C. Allen, J. B. Liu, K. Huang, R. Liu, G. C. He, S. L. Zhao and H. L. Fei, *Adv. Funct. Mater.*, 2022, **32**, 10.
34 M. Acik, G. Lee, C. Mattevi, M. Chhowalla, K. Cho and Y. J. Chabal, *Nat. Mater.*, 2010, **9**, 840–845.
35 M. Acik, G. Lee, C. Mattevi, A. Pirkle, R. M. Wallace, M. Chhowalla, K. Cho and Y. Chabal, *J. Phys. Chem. C*, 2011, **115**, 19761–19781.
36 G. F. Han, F. Li, W. Zou, M. Karamad, J. P. Jeon, S. W. Kim, S. J. Kim, Y. F. Bu, Z. P. Fu, Y. L. Lu, S. Siahrostami and J. B. Baek, *Nat. Commun.*, 2020, **11**, 9.
37 T. Szabo, O. Berkesi, P. Forgo, K. Josepovits, Y. Sanakis, D. Petridis and I. Dekany, *Chem. Mater.*, 2006, **18**, 2740–2749.
38 I. S. Amiinu, X. B. Liu, Z. H. Pu, W. Q. Li, Q. D. Li, J. Zhang, H. L. Tang, H. N. Zhang and S. C. Mu, *Adv. Funct. Mater.*, 2018, **28**, 9.
39 F. F. Zhang, Y. L. Zhu, C. Tang, Y. Chen, B. B. Qian, Z. W. Hu, Y. C. Chang, C. W. Pao, Q. Lin, S. A. Kazemi, Y. Wang, L. Zhang, X. W. Zhang and H. T. Wang, *Adv. Funct. Mater.*, 2022, **32**, 8.
40 K. Sun, R. H. Lu, Y. G. Liu, J. Webb, M. Hanif, Y. F. Zhao, Z. Y. Wang and G. I. N. Waterhouse, *Angew. Chem.*, 2025, **64**, e202416070.
41 C. H. Choi, H. C. Kwon, S. Yook, H. Shin, H. Kim and M. Choi, *J. Phys. Chem. C*, 2014, **118**, 30063–30070.
42 Y. Y. Sun, S. Li, Z. P. Jovanov, D. Bernsmeier, H. Wang, B. Paul, X. L. Wang, S. Kühl and P. Strasser, *ChemSusChem*, 2018, **11**, 3388–3395.